

Effect of cell and microvillus mechanics on the transmission of applied loads to single bonds in dynamic force spectroscopy

V. K. Gupta and C. D. Eggleton

University of Maryland Baltimore County, Baltimore, Maryland 21250, USA

(Received 29 June 2010; revised manuscript received 14 February 2011; published 18 July 2011)

Receptor-ligand interactions that mediate cellular adhesion are often subjected to forces that regulate their detachment via modulating off-rates. Although the dynamics of detachment is primarily controlled by the physical chemistry of adhesion molecules, cellular features such as cell deformability and microvillus viscoelasticity have been shown to affect the rolling velocity of leukocytes *in vitro* through experiments and simulation. In this work, we demonstrate via various micromechanical models of two cells adhered by a single (intramolecular) bond that cell deformability and microvillus viscoelasticity modulate transmission of an applied external load to an intramolecular bond, and thus the dynamics of detachment. Specifically, it is demonstrated that the intermolecular bond force is not equivalent to the instantaneous applied force and that the instantaneous bond force decreases with cellular and microvillus compliance. As cellular compliance increases, not only does the time lag between the applied load and the bond force increase, an initial response time is observed during which cell deformation is observed without transfer of force to the bond. It is further demonstrated that following tether formation the instantaneous intramolecular bond force increases linearly at a rate dependent on microvillus viscosity. Monte Carlo simulations with fixed kinetic parameters predict that both cell and microvillus compliance increase the average rupture time, although the average rupture force based on bond length remains nearly unchanged.

DOI: [10.1103/PhysRevE.84.011912](https://doi.org/10.1103/PhysRevE.84.011912)

PACS number(s): 87.17.Rt, 87.17.Pq, 87.15.ak

I. INTRODUCTION

Understanding the mechanisms of cell adhesion and detachment is of practical significance to the interpretation of *in vitro* force spectroscopy measurements used in determining molecular kinetics, as well as the prediction of adhesion events *in vivo*. Adhesive macromolecules (proteins and oligosaccharides) on the cell surface mediate cell adhesion via multiple noncovalent interactions (van der Waals, hydrogen bonding, hydrophobic, or electrostatic). Cellular adhesion involves complex couplings between biochemistry, structural mechanics, and surface bonding [1]. These intramolecular bonds are often subjected to forces that lead to bond rupture. The force-dependent kinetics of this process, known as off-rates, can be determined by measuring rupture forces under a range of externally applied constant loading rates, an approach popularized by dynamic force spectroscopy (DFS) experiments [2,3]. Currently, the interpretation of force spectroscopy data is tractable under the assumption that the instantaneous force on a molecular bond is equal to the applied load [4]. Although the role of cellular deformability on cell rolling and adhesion is known [5], its role is not accounted for in the analysis of the DFS measurements. The accuracy of off-rate determination is dependent on the dynamics of the molecular bond force. In this paper we investigate the effects of increased cellular deformation by varying cellular material properties and calculating the transmission of the external load to the intermolecular bond using a model of the DFS process.

The dynamic behavior of single-receptor-ligand bonds under force was first discussed by Bell [6], who suggested that bond lifetime is reduced exponentially by an applied load. During recent years, the dynamic behavior of different adhesion bonds under force has been investigated extensively on the level of single molecules by DFS [7]. This field has been pioneered by atomic force microscopy (AFM) experimental studies carried out by Gaub and co-workers [8] and later

put onto a firm theoretical basis by Evans and Ritchie [9]. Force spectroscopy measurements are performed by probing the intermolecular potential with an external mechanical load and noting the ruptures of receptor-ligand bonds [10]. For example, the kinetics of the P-selectin-glycoprotein-ligand-1 (PSGL-1) interaction has been experimentally established by using force spectroscopy measurements [11]. Several different techniques that apply an external mechanical load to adhered cells have been used to probe the intermolecular potential and dissociation kinetics. Dissociation kinetics and forced bond rupture have been investigated theoretically and experimentally using various approaches or assays, e.g., flow chamber [12,13], biomembrane force probe (BFP) [9,14], microneedles [15], AFM [11,16], micropipette aspiration [17,18], optical tweezers [19], magnetic tweezers [20,21], and fluorescence recovery after photobleaching (FRAP) [22].

Single-molecule force spectroscopy is becoming a popular technique for investigating the kinetics of receptor-ligand interaction and single-molecule conformation using recombinant proteins in biophysical research [23]. Force spectroscopy experiments [2] are commonly used to measure the kinetic off-rate of the receptor-ligand bonds by measuring rupture forces. The lifetime of receptor-ligand bonds and force at rupture are stochastic in nature [4]. Receptor-ligand interactions that mediate cellular adhesion are often subjected to forces that regulate their detachment via modulating off-rates [24–26]. Therefore, one should be able to determine off-rates from either bond lifetime or dissociation force measurements [27]. Specifically, bond lifetimes are measured in a range of constant forces. This method was used to obtain the first experimental estimate of $k_{\text{off}}(f)$ for a unimolecular interaction between P-selectin and PSGL-1 [28]. Rupture forces are measured within a range of constant loading rates, a method popularized by the theory of DFS analysis [3]. Bond rupture data are analyzed by constructing rupture force histograms and then

determining the most probable rupture force from nonlinear least-squares fits to a probability distribution. The kinetic off-rates of molecular interactions are extracted from the fit [27]. Recently, Reister-Gottfried *et al.* [24], using simulations and experimental data on the dynamics of membrane adhesion, have shown that for binders confined to surfaces and under conditions of detailed balance, the binding rates are not intrinsic properties of a binding pair, but depend sensitively on the environment factors, namely, membrane fluctuations and the density of binders which affect the nucleation and the effective binding affinity in vesicles. Bond lifetime and rupture force may also be impacted by the formation of tethers at the site of adhesion and observed in vesicles [29,30], endothelial cells [31], and the microvilli of polymorphonuclear leukocytes (PMNs) [32] which can stretch to form tethers rather than allow adhesive interactions to rupture [33].

Cellular adhesion plays a pivotal role in diverse biological processes, including thrombosis [34], tumor metastasis [35], arteriosclerosis [36], and inflammation [37,38]. Changes in cell adhesion can be the defining event in a wide range of diseases, including cancer [39], arthritis [40], osteoporosis, and atherosclerosis [41]. Adhesion structures in living cells can grow and strengthen under force [42]. The force-induced adhesion strengthening can occur purely because of the thermodynamic response to the elastic deformation of the membrane [42,43]. Cell adhesion-detachment is determined by the balance between the adhesive forces generated by the membrane-bound receptor-ligand interactions and external forces that may arise from applied loads in experiment or from the physiological environment, for example, hemodynamics.

Kinetic on-rates and off-rates play a crucial role in determining adhesive events that are crucial to the immune response. The recruitment of free-flowing PMNs to the sites of infection, inflammation, or tissue injury is a key step in the body's inherent immune response [44]. The recruitment of PMNs to these sites involved a multistep process with the sequential interaction of distinct adhesion molecules on PMN and endothelium cell (EC) surfaces [45]. This three-step process is initiated by selectin-mediated PMN tethering and rolling along the EC surface, followed by integrin-dependent firm adhesion leading to eventual extravasation into the tissue space [41]. Rolling adhesion is the result of nearly simultaneous bond rupture and bond formation on the upstream and downstream side of the cell surface, due to the fast association and dissociation kinetics of selectins [38,46]. A rolling velocity that is smaller than the velocity of a freely moving cell allows leukocytes to efficiently survey for chemokine molecules that indicate the presence of an infection. Bond formation with adhesion receptors from the integrin family [47] leads to firm adhesion, a precursor for the eventual extravasation of the leukocyte into the tissue space [41]. This cascade of highly regulated molecular events is modulated by local circulatory hemodynamics and the mechanical and kinetic properties of involved adhesion molecules. Not only fast on- and off-rates, but also a high tensile strength of the receptor-ligand bond and anchoring of the receptor and ligand to the cytoskeleton, appear necessary to mediate leukocyte tethering and rolling at physiological shear stresses [28]. Receptor-ligand mediated cell rolling and adhesion has been systematically investigated

in computational studies pioneered by Hammer and co-workers [44,48–50] using an adhesive dynamics algorithm in which the cell is idealized as a hard sphere and rolling results from a balance of forces and torques on the cell due to hydrodynamic shear and receptor-ligand bonds. The adhesive dynamics algorithm has successfully reproduced the experimentally observed “stop and go” motion of rolling cells. However, it does not account for cell deformation that has been experimentally shown to critically affect the rolling behavior of cells. To overcome this limitation, Jadhav *et al.* [5] developed a more realistic three-dimensional (3D) model simulating receptor-mediated rolling of a deformable cell on a selectin-coated surface in a linear shear field. Recently Korn and Schwarz [51,52] developed a different variant of the adhesive dynamics algorithm which, in contrast to earlier approaches, fully resolves the spatial positions of the receptors on the sphere and the ligands on the wall. Using this approach, they were able to predict the efficiency of initiating cell adhesion in shear flow as a function of the density and geometry of the receptor and ligand patches [51,52]. They further extended their work to include the diffusive motion of cells resulting from thermal fluctuations to fully resolve the spatial positions of receptors and ligands and calculated the state diagrams as a function of the on- and off-rate [47].

Single-molecule pulling experiments provide a powerful tool to measure the kinetic off-rates of intermolecular bonds that control the immune response. Given the complexity of the adhesive response to the mechanical and chemical environment, the question as to whether the measured kinetic off-rate is the same when the bond is formed between adhesion molecules residing on solid beads or on live cells has been addressed through the practice of live cell experimentation [23]. Recently Dudko *et al.* [53] presented a methodology that unifies several previous approaches [6,9,54,55] and allows one to extract three parameters describing a one-dimensional (1D) landscape from kinetic data collected under different forces or pulling speeds under the assumption that the instantaneous force on a molecular bond is equal to the applied load. These three parameters describe the height of the barrier and its distance from the initial state along the pulling coordinate and the intrinsic rate [56]. However, using living cells instead of recombinant proteins [57] ensures that the natural orientation, surface density, and post-translational modifications of the probed receptors are physiological and that their regulated attachment to the cytoskeleton can occur [23]. Moreover, using living cells ensures that transmembrane receptors can still interact with the cytoskeleton via interactions mediated by cytoplasmic proteins binding the cytoplasmic domain of the receptors and ensures that cell signaling pathways can occur [23].

It is critical to understand the physics of DFS involving deformable cells. In this work, we model the DFS process using various micromechanical models of two cells adhered by a single (L-selectin-PSGL-1) bond. In our model two nearly adjacent PMN cells are allowed to adhere by a single bond. Once adhered, equal and opposite forces on the surface of each cell are applied along the line connecting the end of the bond causing stretching and eventually bond rupture (see Fig. 1). Idealized cells are modeled as solid spheres and elastic capsules, while the microvillus is modeled as a solid and a

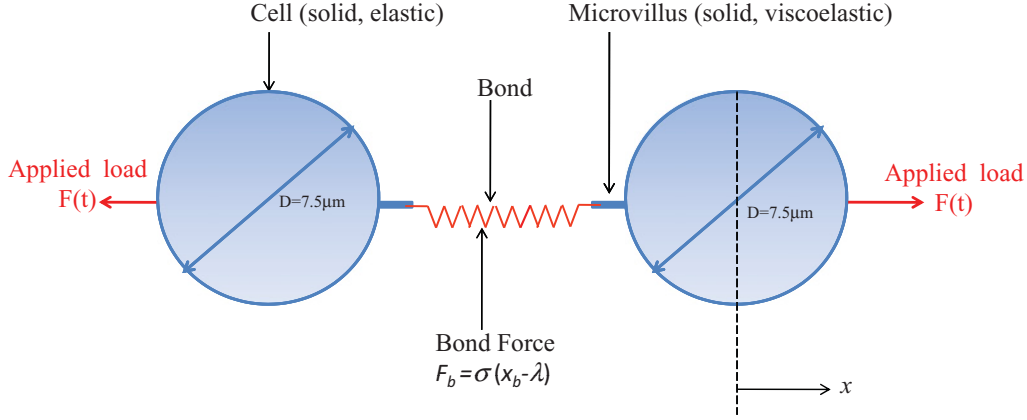


FIG. 1. (Color) Schematic of two PMN cells detachment (not drawn to scale) through binding between PSGL 1 (receptor) and L selectin (ligand) molecules concentrated on the tip of PMN microvillus.

viscoelastic material with an extensible elastic regime and a viscous tether regime. The simulations demonstrate how microvillus and cellular deformation modulate the transmission of the applied force to the molecular bond and we show how this affects bond lifetimes.

II. COMPUTATIONAL METHOD

The adhesion and detachment of two deformable PMNs suspended in a Newtonian fluid is simulated by simultaneously: (1) solving the Navier-Stokes (NS) equation by the immersed boundary method (IBM) for motion of elastic capsules suspended in a Newtonian fluid; (2) solving the constitutive equation using the finite-element method for the neo-Hookean membrane of the spherical capsule [58]; and (3) simulating the formation and breakage of receptor-ligand bonds using the Monte Carlo method with kinetic rate constants based on the Hookean spring model [44,59].

A. Immersed boundary method

To account for the deformability of PMN cells, an elastic membrane is used because it has been shown to better approximate the PMN surface as compared to surface tension in a viscous drop model of the leukocyte [60]. The two PMN cells modeled as 3D elastic capsules each containing a Newtonian fluid of density ρ and viscosity μ are placed in a medium fluid with the same density and viscosity. As the two cells adhere to each other, deformation and movement of the cells could generate fluid flow both inside and around the cells. The fluid flow both outside and inside the cells is governed by the NS momentum balance equation,

$$\rho \frac{\partial \mathbf{u}(\mathbf{x})}{\partial t} = -\nabla p(\mathbf{x}) + \mu \nabla^2 \mathbf{u}(\mathbf{x}) + \mathbf{F}(\mathbf{x}), \quad (1)$$

and the continuity equation written for incompressible fluid,

$$\nabla \cdot \mathbf{u}(\mathbf{x}) = 0, \quad (2)$$

where $\mathbf{u}(\mathbf{x})$ is the velocity vector at position $\mathbf{x}(x_1, x_2, x_3)$, p is pressure, and $\mathbf{F}(\mathbf{x})$ is the total force exerted by the elastic membrane deformation and receptor-ligand bonds onto the fluid.

The fluid flow along with the deformation of the cell membrane is simulated using the IBM [61]. In the IBM, the computational domain comprises a Lagrangian triangular finite-element 3D grid $\mathbf{X}(X_1, X_2, X_3)$ that tracks cell membrane motion and deformation and an Eulerian Cartesian fluid 3D grid $\mathbf{x}(x_1, x_2, x_3)$ for solving fluid motion both outside and inside the cells [58,62].

In the IBM, at the beginning of each time step t , the total force exerted by the elastic cell membrane deformation and receptor-ligand bonds is calculated. This force, denoted by $F(\mathbf{X})$ and located at immersed boundary nodes \mathbf{X} , is distributed to the nearby fluid grid nodes \mathbf{x} , using an adequately chosen function $D_h(\mathbf{x})$,

$$F(\mathbf{x}) = \sum F(\mathbf{X}) \cdot D_h(\mathbf{x}) \text{ for } |\mathbf{X} - \mathbf{x}| \leq 2h, \quad (3)$$

where h is the uniform grid spacing and the 3D discrete δ function $D_h(\mathbf{x})$ defined by

$$D_h(\mathbf{x}) = \delta_h(x_1/h) \delta_h(x_2/h) \delta_h(x_3/h), \quad (4)$$

is a product of 1D discrete δ functions given by [see Eq. (6.27) in Ref. [63]]

$$\delta_h(r) = \begin{cases} \frac{3-2|r|+\sqrt{1+4|r|-4r^2}}{8}, & |r| \leq 1, \\ \frac{5-2|r|+\sqrt{-7+12|r|-4r^2}}{8}, & 1 \leq |r| \leq 2, \\ 0, & 2 \leq |r|, \end{cases}$$

where r is a dimensionless scalar quantity. The fluid velocity $\mathbf{u}(\mathbf{x})$ for the next time step $t + \Delta t$ is obtained by applying periodic boundary conditions on the velocity and pressure along all three axes for efficient solution of the NS equation coupled with the continuity equation by fast Fourier transform [61]. The “no-slip” or continuity of velocity condition at the elastic membrane surface is enforced by moving the respective membrane nodes with the local fluid velocity. The velocity $\mathbf{U}(\mathbf{X})$ of a cell membrane node \mathbf{X} is the weighted sum of the velocities at the fluid grid nodes \mathbf{x} :

$$\mathbf{U}(\mathbf{X}) = \sum h^3 \mathbf{u}(\mathbf{x}) \cdot D_h(\mathbf{x}) \text{ for } |\mathbf{X} - \mathbf{x}| \leq 2h. \quad (5)$$

At the end of each time step $t + \Delta t$, the position of the nodes of the elastic cell membrane is updated using the following relation,

$$\mathbf{X}_{t+\Delta t} = \mathbf{X}_t + \Delta t \times \mathbf{U}(\mathbf{X}_t). \quad (6)$$

This leads to deformation of the elastic elements, and the forces due to the elastic cell membrane deformation and receptor-ligand bonds are recalculated and added to the NS equation at the beginning of the next time step. The entire scheme is repeated to march forward in time.

B. Membrane constitutive equation

The two PMN cells are approximated as spherical capsules with an elastic membrane in an initial strain-free state, which is discretized into flat triangular elements. The neo-Hookean membrane material is assumed to be initially incompressible and isotropic. Hence, the strain energy W_δ can be expressed as a function of only the in-plane principal stretch ratios λ_1 and λ_2 [58,64,65] as follows,

$$W_\delta = \frac{E\delta}{6} \left(\lambda_1^2 + \lambda_2^2 + \frac{1}{\lambda_1^2 \lambda_2^2} - 3 \right), \quad (7)$$

where E is the Young's modulus for the elastic material and δ is the membrane thickness. The finite-element implementation of the membrane force $F(\mathbf{x})$ calculation is based on the methodology developed by Charrier *et al.* [64]. To obtain the forces acting at the discrete nodes of the membrane surface, we discretized the membrane into triangular finite elements. These forces are then distributed onto the fluid grid as described above in Eq. (3). For the given relative displacement of the three nodes of an element, its state of strain (λ_1 and λ_2) is obtained. The forces that are required to maintain the element in a given state of strain or stress are determined by the material properties of the element. We used the principle of virtual work to calculate the forces at the three nodes of an element. The resultant force $F(\mathbf{X})$ on membrane node \mathbf{X} is simply the sum of the forces exerted by the triangular elements attached to that node. An equal and opposite force acts on the fluid as described by IBM. More details of the numerical implementation can be found in Refs. [58] and [64].

C. Monte Carlo simulation of receptor-ligand interactions

We model the bonds between adhesion molecules (receptor and ligand) located on the microvillus of PMN cells as Hookean springs, so the chemical force on each cell due to each bond \mathbf{F}_b is given by

$$\mathbf{F}_b = \sigma(\mathbf{x}_m - \lambda), \quad (8)$$

where σ is the bond spring constant, \mathbf{x}_m is the stressed bond length, and λ is the equilibrium bond length. According to the Hookean spring (Dembo) model, the forward rate constant k_f for ligand-receptor interactions is given by [59]

$$k_f = k_f^0 \exp \left[-\frac{\sigma_{ts}(x_m - \lambda)^2}{2k_b T} \right], \quad (9)$$

and the reverse rate constant k_r is given by [59]

$$k_r = k_r^0 \exp \left[\frac{(\sigma - \sigma_{ts})(x_m - \lambda)^2}{2k_b T} \right], \quad (10)$$

where k_f^0 and k_r^0 are the forward and reverse rate constants at an equilibrium distance λ , T is the absolute temperature, k_b is the Boltzmann constant, and σ_{ts} represents the spring constant in the transition state. Besides the Dembo model [59] for the rate of bond formation and rupture, there are Bell [6,9] and Two-pathway [66] models. Data for L-selectin and PSGL-1 single-bond rupture under loading was analyzed in Ref. [67], where it was concluded that these bonds enter the slip regime when the loading rate is greater than 200 pN/s. In our simulation we used the slip bond model given by Eqs. (9) and (10) to simulate adhesion and detachment of two PMN cells.

We use a Monte Carlo simulation to incorporate the stochastic nature of the receptor-ligand interactions. In the simulation during a time interval Δt , the probability (P_b) that a ligand will bind with its complementary receptor is given by [44]

$$P_b = 1 - \exp(-k_f \Delta t). \quad (11)$$

Similarly the probability for bond rupture is given by [44]

$$P_r = 1 - \exp(-k_r \Delta t). \quad (12)$$

At each time step, the probabilities of bond formation and rupture are compared to random numbers (P_{ran1} and P_{ran2}) lying between 0 and 1. $P_b > P_{\text{ran1}}$ indicates bond formation whereas $P_r > P_{\text{ran2}}$ indicates bond rupture.

D. Microvillus deformability

It has been observed experimentally that under the application of a pulling force exerted by the bond, the microvillus stretches as described by Shao and co-workers [32]. When the microvillus is viscoelastic it can be extended and may form a tether when the force is greater than 45 pN [32]. The viscoelastic nature of the microvillus is captured by modeling it as a Hookean spring if the force is < 45 pN (extension regime) and as a long thin membrane cylinder (a tether) for forces > 45 pN (tethering regime). In the extension regime, the force exerted by the bond on the microvillus (F_m) is given by

$$F_m = \sigma_m(L_m - L_{m0}), \quad (13)$$

whereas in the tethering regime, it is given by

$$F_m = F_{m0} + \mu_m \frac{dL_m}{dt}, \quad (14)$$

where F_{m0} is the threshold force between the two regimes, σ_m is the microvillus spring constant, μ_m is the tether effective viscosity, L_m is the microvillus length at any time t , and L_{m0} is the resting microvillus length.

Assuming that the bond between a pair of microvillus between two cells has the same direction vector as that of the bound microvillus, the system can be likened to a Hookean spring (receptor-ligand bond) in series with either another Hookean spring (σ_m) or a tether (μ_m). F_m can be expressed as a function of the resting bond length (λ) as follows,

$$F_m = \sigma[L_t - (2L_m + \lambda)], \quad (15)$$

where L_t is the distance between the two bases of the microvillus on the two cell surfaces, i.e., $L_t = 2L_m + L_b$,

where L_b is the bond length at any time t . Based on the magnitude of the force acting on the microvillus, its length can be obtained by solving the above equations for each regime. In the extension regime it is given by

$$L_m = \frac{1}{(\sigma_m + 2\sigma)} [\sigma_m L_{m0} + \sigma \{L_t - \lambda\}], \quad (16)$$

whereas in the tethering regime it is given by

$$\mu_m \frac{dL_m}{dt} + 2\sigma L_m = \sigma [L_t - \lambda] - F_{m0}. \quad (17)$$

E. Micromechanical model of detachment of inelastic PMN cells

Considering the two PMN cells as inelastic, we can write an analytical expression for a time-varying bond stretch. Due to symmetry we consider only one cell in writing the following momentum balance:

$$\rho \frac{4}{3} \pi R^3 \frac{d^2x}{dt^2} = F(t) - \sigma x - 6\pi \mu R \frac{dx}{dt}, \quad (18)$$

where x is the displacement of cell center as shown in Fig. 1. Letting $a = \rho \frac{4}{3} \pi R^3$, $b = 6\pi \mu R$, and $c = \sigma$, the above equation becomes

$$a \frac{d^2x}{dt^2} + b \frac{dx}{dt} + cx = F(t). \quad (19)$$

For $F = R_f t$, where R_f is the loading rate, the general solution is

$$x(t) = c_1 \exp(\alpha t) + c_2 \exp(\beta t) + \frac{R_f}{c} \left(t - \frac{b}{c} \right), \quad (20)$$

where

$$\alpha = \frac{-b + \sqrt{b^2 - 4ac}}{2a}, \quad \beta = \frac{-b - \sqrt{b^2 - 4ac}}{2a}, \quad (21)$$

and c_1, c_2 are constants of integration which can be determined using initial conditions $x(0) = x'(0) = 0$. Note that $x_b(t) = x(t)$ when the microvillus is solid, where $x_b(t)$ is the bond stretching. When the microvillus is viscoelastic, it can be extended (deform) and may form a tether when the force is greater than 45 pN [32]. In the extension regime the general solution for $x_b(t)$ is still given by Eq. (20) but with modified $a = (1 + \frac{\sigma}{\sigma_m}) \rho \frac{4}{3} \pi R^3$, $b = (1 + \frac{\sigma}{\sigma_m}) 6\pi \mu R$, and $c = \sigma$. Similarly, in the tether regime the general solution for $x_b(t)$ is still given by Eq. (20) but with modified $a = \rho \frac{4}{3} \pi R^3$, $b = \frac{\sigma}{\mu_m} \rho \frac{4}{3} \pi R^3 + 6\pi \mu R$, and $c = \sigma + \frac{\sigma}{\mu_m} 6\pi \mu R$. Thus, knowing $x_b(t)$ we can simulate the detachment of receptor-ligand bond as a function of loading rate using the Monte Carlo method [44].

F. Simulating cell-cell breakup via applying external force

In our simulation experiments as soon as a (L-selectin and PSGL-1) bond between the two cells is formed, we apply an equal and opposite force $F(t) = R_f t$ on the surface of each cell in the direction causing bond stretching and eventually bond rupture. Note that the two cells are pulled apart along the line connecting their centers. Bonds break due to the stochastic nature, with the lowest probability at equilibrium, according to Eqs. (10) and (12). The probability for bond rupture P_r

increases as the separation distance between the two cells increases. In our simulation experiment at any instant of time we first determine the probability for bond rupture P_r given by Eq. (12). We then establish whether or not bond rupture occurs according to the criterion described above. Note that this simulation requires solving fluid flow equations by IBM since applying an equal and opposite force on the surface of each cell along the line connecting their centers will lead to deformation and flow inside and around the cells. This solid-fluid interaction is best handled by the methodology described above. To circumvent any numerical instability, the force $F(t)$ is not applied at a point on each cell surface, rather we distribute it equally among all the membrane nodes lying on the cell surface at a distance z from the center of each cell such that $0.8R \leq |z| \leq R$, where R is the radius of each cell [68]. The new nodal forces are then distributed to the nearby fluid grid nodes in addition to the elastic forces using the discrete delta function as discussed before. The fluid forces are then added to the NS equation. The effect of distributing the forces into the fluid is to initiate flow that leads to additional viscous forces, which in turn pulls the two cells apart and deforms them due to the elasticity of the membrane. Once the bond is ruptured the two cells separate from each other to a distance where further bond (re)formation is impossible, and then the simulation is terminated.

G. Model and computational parameters

We simulated adhesion and detachment of two elastic PMN cells using the parameter values listed in Table I unless stated otherwise. Two 3D elastic stress-free capsules representing two PMN cells are placed in the 3D fluid computational domain of a box of size $8R \times 8R \times 8R$. The center-to-center distance between the two cells is $8.25 \mu\text{m}$. A time step of 10^{-7} s is used in all these simulations. A limitation of our 3D model is that the viscosity of the fluid inside the capsule is the same as that of the medium fluid. Therefore, membrane stiffness values (see Table I) are chosen to obtain cell deformation observed in experimental studies [69] and are in the same range as the surface tension values used in the two-dimensional (2D) viscous drop model of PMN [70]. However, the membrane stiffness values are one order of magnitude higher than the previously reported cortical tension values (0.03 dyn/cm) estimated from PMN aspiration experiments [71] to compensate for the absence of viscoelastic resistance from the cytoskeleton. A detailed ultrastructural study of Bruehl *et al.* [72] has shown that the actual length of microvilli varies from 0.15 to $0.7 \mu\text{m}$. In our work we use the average length of microvilli as $0.35 \mu\text{m}$. Further, Weinbaum and colleagues [73] have predicted the presence of sizable compressive forces on the tips of microvilli, especially on the small population (5%–10%) of long microvilli ($>0.5 \mu\text{m}$), due to gravitational hydrodynamics interactions with a wall. We do not consider compressive forces since our rupture simulations apply a tensile load on microvilli. Note that the transition state depends on the applied load [74]. In this work all our simulation results correspond to a constant σ_{ts} . In our model for PMN binding and rupture, the microvilli are modeled both as solid cylinders that do not deform under force and as deformable, in which case they stretch under the application

TABLE I. Parameter values used in the model.

Parameter	Definition	Value	Reference
R	PMN radius	$3.75 \mu\text{m}$	[76]
L_{mv}	Length of microvillus	$0.35 \mu\text{m}$	[32]
λ	Receptor-ligand bond length	$0.07 \mu\text{m}$	[62]
k_f^0	Unstressed on rate	3 s^{-1}	[76]
k_r^0	Unstressed off-rate	3 s^{-1}	[76]
σ	Spring constant	4 dyn/cm	[76]
σ_{ts}	Transition-state spring constant	3.96 dyn/cm	[44]
E_h	Membrane stiffness	$0.3\text{--}3.0 \text{ dyn/cm}$	[62]
σ_m	Microvillus spring constant	$43 \text{ pN}/\mu\text{m}$	[32]
μ_m	Effective viscosity of tether	$11 \text{ pN s}/\mu\text{m}$	[32]
F_{m0}	Threshold force	45 pN	[32]
μ	Fluid viscosity	0.8 cP	
ρ	Fluid density	1 g/cm^3	
T	Temperature	310 K	

of a pulling force [32]. We also assume that elastic capsules have a smooth membrane and do not account for the roughness due to the presence of microvilli on the surface. The initial van der Waals attraction between a pair of microvillus separated by $0.05 \mu\text{m}$ is $\sim 0.001 \text{ pN}$ [see Eq. (A9) in Ref. [44]], which is very small compared to the tensile load on a microvillus, and hence we do not consider van der Waals attraction in our model simulation. Similarly, the electrostatic and steric stabilization forces have been neglected because these forces exist in biological systems at distances from 50 to 250 \AA [44].

III. RESULTS

A. Intermolecular bond force for various cell and microvillus models

Figure 2 shows the evolution of applied load and intermolecular bond force with time obtained from various cell and microvillus models at $R_f = 10^5 \text{ pN/s}$ for the model parameters listed in Table I. The applied load shown as a solid line increases linearly with time simply because $F = R_f t$. On the other hand, the intermolecular bond force increases nonlinearly with time for all the models considered in this work, except for the case when both the cell and microvillus are modeled as solid materials. In this case the intermolecular bond force increases nearly linearly with time, as shown by the dashed lines in Fig. 2. However, there is a small time lag of $\sim 20 \mu\text{s}$ due to the hydrodynamic drag on the solid sphere. Now, consider the case of a solid cell with a viscoelastic microvillus. The nonlinearity in intermolecular bond force with time is highly pronounced. In the extension regime, where the microvillus is modeled as a linear spring, there is a significant time lag between the applied load and the bond force. However, once the microvillus deformation crosses from the extension regime to the tether regime, there is an abrupt (nearly discontinuous) change in the derivative with respect to time of the intermolecular bond force, after which it increases nearly linearly with time and approaches the instantaneous applied load, as shown by the dashed-dotted line (b) in Fig. 2. The corresponding data for the intermolecular bond force leveled (c)–(h) is obtained from a 3D IBM simulation of

elastic cells at the same loading rate. The intermolecular bond force obtained from the 3D IBM simulation of an elastic cell with a solid microvillus is shown as dashed lines (c)–(e), while that of an elastic cell with deformable microvillus is shown as dashed-dotted lines (f)–(h) in Fig. 2 for three different values of membrane stiffness $E_h = 3.0, 1.2,$ and 0.3 dyn/cm . It is seen that the 3D IBM simulations of elastic cells also predict a nonlinear increase in intermolecular bond force with time. Further, it is seen that, irrespective of the cell and microvillus model used, the intermolecular bond force does not experience the instantaneously applied load at any instant of time and is always lower than the applied load. The difference in applied load and the intermolecular bond force is lowest when both the cell and microvillus are

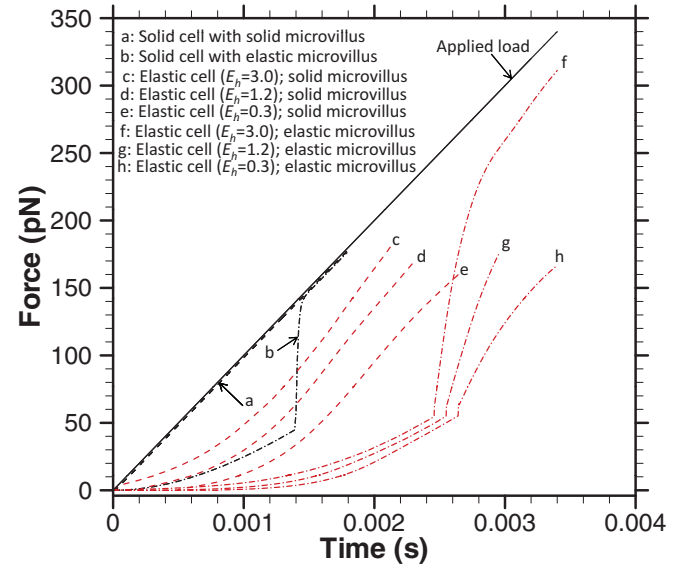


FIG. 2. (Color online) Time variation of applied force (solid line), intermolecular bond force with solid microvillus (dashed line), and intermolecular bond force with deformable microvillus (dashed-dotted line) obtained from the micromechanical model and IBM simulations at $R_f = 10^5 \text{ pN/s}$ for the model parameters listed in Table I.

modeled as solid materials, while it is the largest when both the cell and microvillus are modeled as elastic materials. In the long-term limit, if the bond is not allowed to break, then the instantaneous intermolecular bond force tends to the applied load, as seen from dashed-dotted line (f) in Fig. 2. This is true for the experimentally measured effective viscosity of tether ($\mu_m = 11$ pNs/ μ m). However, if we artificially decrease the tether viscosity by an order of magnitude while keeping other parameters fixed, we see from Fig. 5(c) that the instantaneous intermolecular bond force does not tend to the applied load.

B. Mechanism of force transmission

It is observed from Fig. 2 that as we increase membrane elasticity (decrease E_h) there is a time lag in force transmission from the cell to the bond, i.e., the intermolecular bond force does not increase instantaneously once an external force ($R_f = 10^5$ pN/s) is applied to the cell. The lag in force transmission from the cell to the bond increases as we increase the membrane elasticity. This is best illustrated in the animations 1–3 given in the supplemental material [75]. In these animations we show the evolution of cell shape once the external force is applied on the cell surface. These animations show that the time lag in force transmission from the cell surface to the bond depends on membrane elasticity. We also obtained the corresponding animations from simulations of elastic cells with elastic microvilli. They are given by movies 4–6 in the supplemental material [75]. These animations

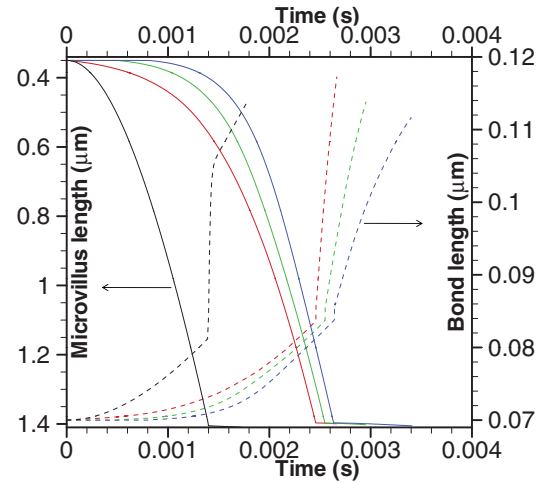


FIG. 3. (Color) Time variation of microvillus (black solid line) length and bond (black dashed line) length obtained from micromechanical model simulation at $R_f = 10^5$ pN/s. The corresponding data in color is obtained from the IBM simulation of elastic cell with elastic microvillus at $R_f = 10^5$ pN/s for $E_h = 3.0$ dyn/cm (red line), $E_h = 1.2$ dyn/cm (green line), and $E_h = 0.3$ dyn/cm (blue line) for the model parameters listed in Table I.

show that microvillus extension and tether formation further contribute to this time lag, as seen in Fig. 2. These simulations demonstrate that whole cell and microvillus deformation alter

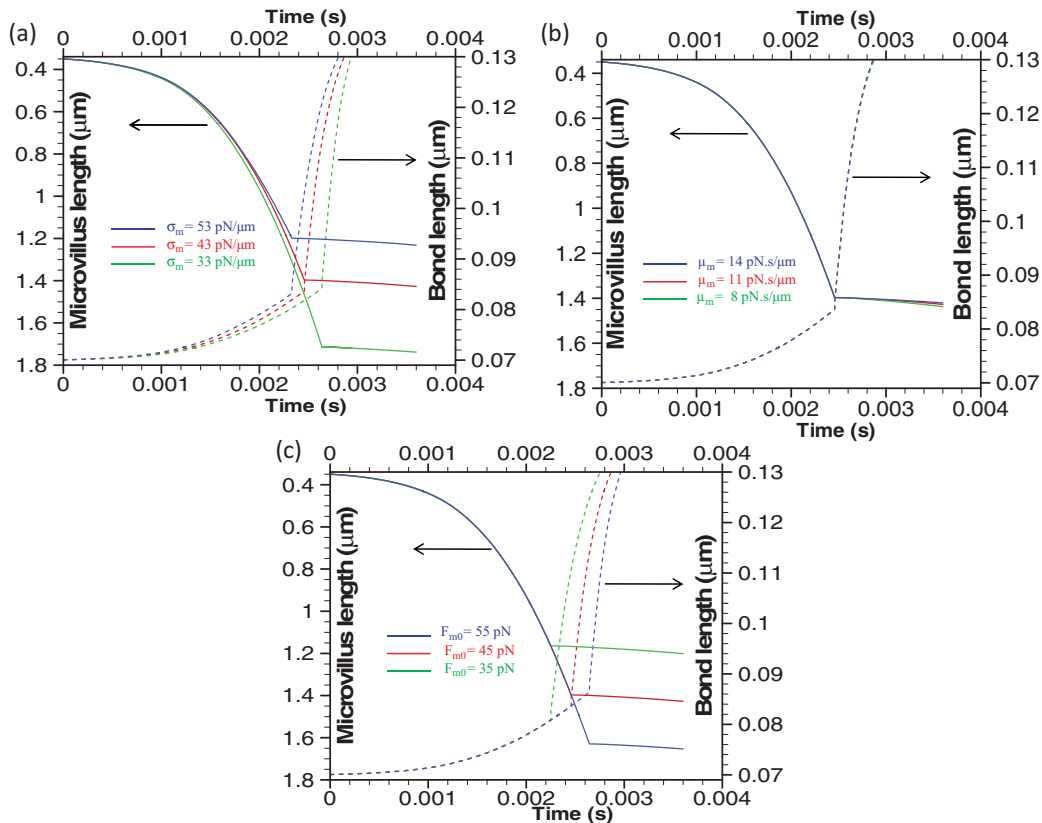


FIG. 4. (Color) Effect of varying microvillus viscoelastic model parameter (a) σ_m , (b) μ_m , (c) F_{m0} on the evolution of microvillus (solid line) length and bond (dashed line) length obtained from the IBM simulation of elastic cell ($E_h = 3.0$ dyn/cm) at $R_f = 10^5$ pN/s for the model parameters listed in Table I.

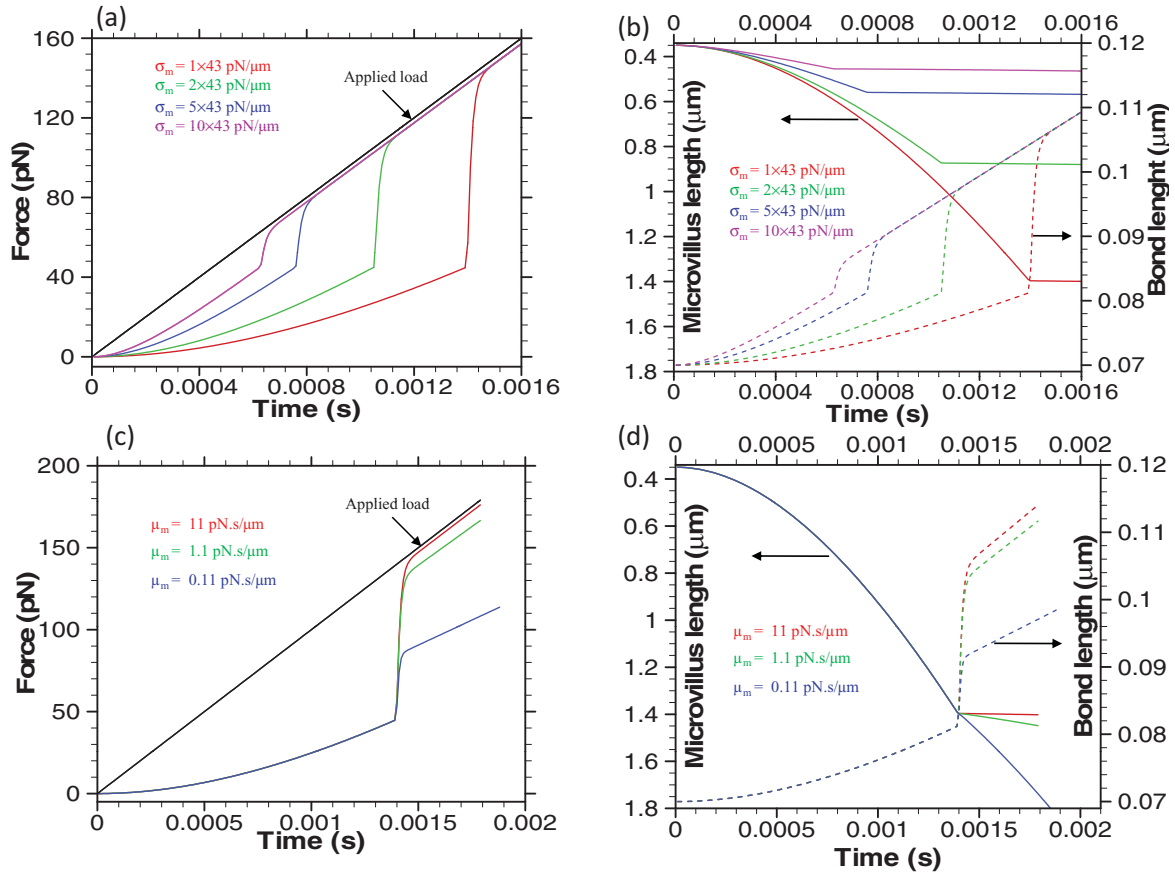


FIG. 5. (Color) Effect of varying microvillus viscoelastic model parameter σ_m on the evolution of (a) intermolecular bond force, (b) microvillus (solid line) length and bond (dashed line) length, and effect of varying microvillus viscoelastic model parameter μ_m on the evolution of (c) intermolecular bond force, (d) microvillus (solid line) length and bond (dashed line) length obtained from the micromechanical model simulation at $R_f = 10^5$ pN/s for the model parameters listed in Table I.

force transmission to the intramolecular bond. In general, the more extensible the cell, the larger is the time lag between the applied load and the bond force.

C. Role of microvillus mechanics on bond force

In order to further investigate the mechanics of force transmission through the microvillus, we show in Fig. 3 the

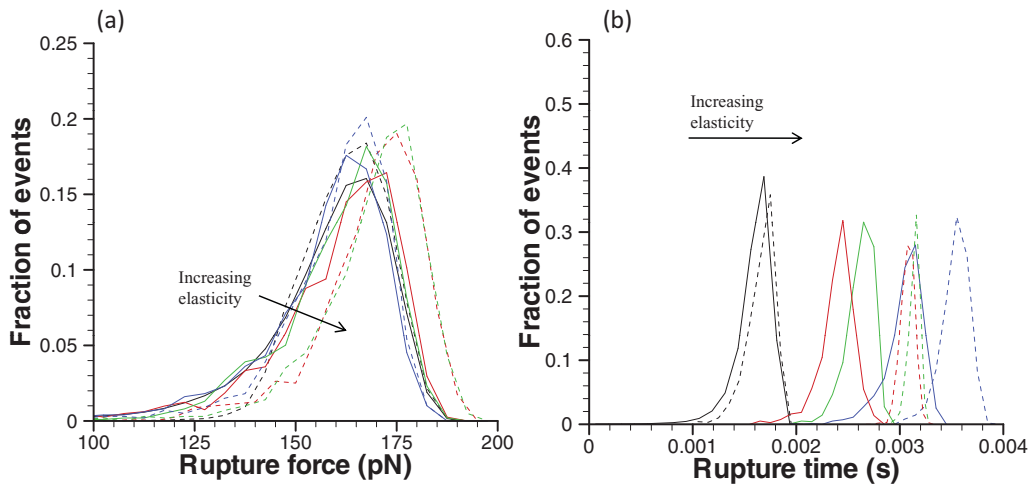


FIG. 6. (Color online) Histograms of (a) rupture force and (b) rupture time obtained from the micromechanical model simulation of solid cell and IBM simulation of elastic cell with solid microvillus (solid line) and elastic microvillus (dashed line) at $R_f = 10^5$ pN/s for the model parameters listed in Table I.

TABLE II. Average rupture force and rupture time at $R_f = 10^5$ pN/s.

Cell model	Microvillus model	Average rupture force (pN)	Average rupture time (μ s)	Tether contribution
Solid	Solid	157.69	1593.2	NA
Solid	Elastic	161.68	1797.3	99.5%
Elastic ($E_h = 3.0$ dyn/cm)	Solid	159.01	2393.6	NA
Elastic ($E_h = 1.2$ dyn/cm)	Solid	159.20	2617.2	NA
Elastic ($E_h = 0.3$ dyn/cm)	Solid	156.26	3046.0	NA
Elastic ($E_h = 3.0$ dyn/cm)	Elastic	174.56	3115.5	99.2%
Elastic ($E_h = 1.2$ dyn/cm)	Elastic	174.82	3258.7	99.0%
Elastic ($E_h = 0.3$ dyn/cm)	Elastic	175.37	3539.3	99.3%

time variation of the microvillus length and the bond length obtained for a solid cell model and from the IBM simulations of elastic cells with viscoelastic microvilli at $R_f = 10^5$ pN/s for $E_h = 3.0$ dyn/cm (red line), $E_h = 1.2$ dyn/cm (green line), and $E_h = 0.3$ dyn/cm (blue line) for the model parameters listed in Table I. The increase in length of microvilli follows two regimes, namely, the extension and tethering regime. It is seen that for a solid cell or membrane with a given elasticity (E_h), the length of the microvillus increases from the resting microvillus length ($0.35 \mu\text{m}$) to $\sim 1.4 \mu\text{m}$ in the extension regime. At this length the force in a microvillus equals the threshold force for transition to the tether regime. Once the microvillus enters the tethering regime, the length of the microvillus increases relatively slowly, while the bond length increases relatively quickly, in comparison to the extension regime. In the microvillus extension regime, the instantaneous force exerted on the molecular bond depends not on the applied load, but on the instantaneous length and extension of the microvilli. Thus, the time lag seen in Fig. 2 in the extension regime appears because force is transmitted to the bond through microvilli stretching. Further, it is seen from Fig. 3 that there is a time lag before the microvillus actually starts extending, i.e., the microvillus length does not increase instantaneously once an external force ($R_f = 10^5$ pN/s) is applied to the cell surfaces. The delay in microvillus extension increases as we increase the membrane elasticity (decreasing E_h). Once again it is seen that the applied force is not instantly transmitted from the cell surface to the bond. However, once the microvillus mechanics crosses from the extension into the tethering regime, the force exerted by the microvillus on the bond now depends on the rate of microvillus extension.

In this regime the force is transmitted rapidly to the bond with a relatively small extension of the microvillus, as seen in Fig. 3. In the tethering regime the rate of microvillus length increase with time is $\sim 0.09 \mu\text{m/s}$ while that of the bond is $\sim 60 \mu\text{m/s}$ (assuming a linear increase with time for the sake of argument). To investigate the effects of the microvillus model parameters on force transmission, we varied the microvillus spring stiffness (σ_m), microvillus viscosity (μ_m), and threshold force (F_{m0}), while keeping all other parameters fixed to their values in Table I. Here, the variation in microvillus model parameters is of the magnitude of the standard deviations reported in Ref. [32]. It is seen in Fig. 4(a) that for the small variations in microvillus stiffness (25%) the net effect is to alter the transition to the tether regime (a stiffer microvilli transition sooner). A small variation of microvillus viscosity has a negligible effect on force transmission, as seen in Fig. 4(b), while the effect of altering the threshold force seen in Fig. 4(c) is to alter the transition to the tether regime (a lower threshold force microvilli transition sooner). These small variations in microvillus parameters based on experimental measurements do not have a significant effect on the force transmission to the bond. In order to better understand the role of the microvillus parameters in force transmission to the molecular bond, we separately vary the spring stiffness and tether viscosity by an order of magnitude while keeping other parameters fixed. We see in Fig. 5(a) that microvillus stiffness has a major influence on the initial time lag between the applied load and the bond force. Stiffer microvilli transfer force faster. Figure 5(b) clearly shows that this is because more compliant microvilli must be extended to a longer length to exert the same force, and this extra extension requires a

TABLE III. Effect of varying microvillus viscoelastic model parameters on average rupture force and rupture time at $R_f = 10^5$ pN/s for elastic cell ($E_h = 3.0$ dyn/cm).

σ_m (pN/ μm)	μ_m (pN s/ μm)	F_{m0} (pN)	Average rupture force (pN)	Average rupture time (μ s)	Tether contribution
33	11	45	176.10	3289.4	99.0%
43	11	45	174.56	3115.5	99.2%
53	11	45	173.23	2963.6	99.1%
43	8	45	174.49	3124.6	99.2%
43	11	45	174.56	3115.5	99.2%
43	14	45	174.67	3103.8	99.2%
43	11	35	172.30	2968.5	99.3%
43	11	45	174.56	3115.5	99.2%
43	11	55	176.39	3236.0	99.1%

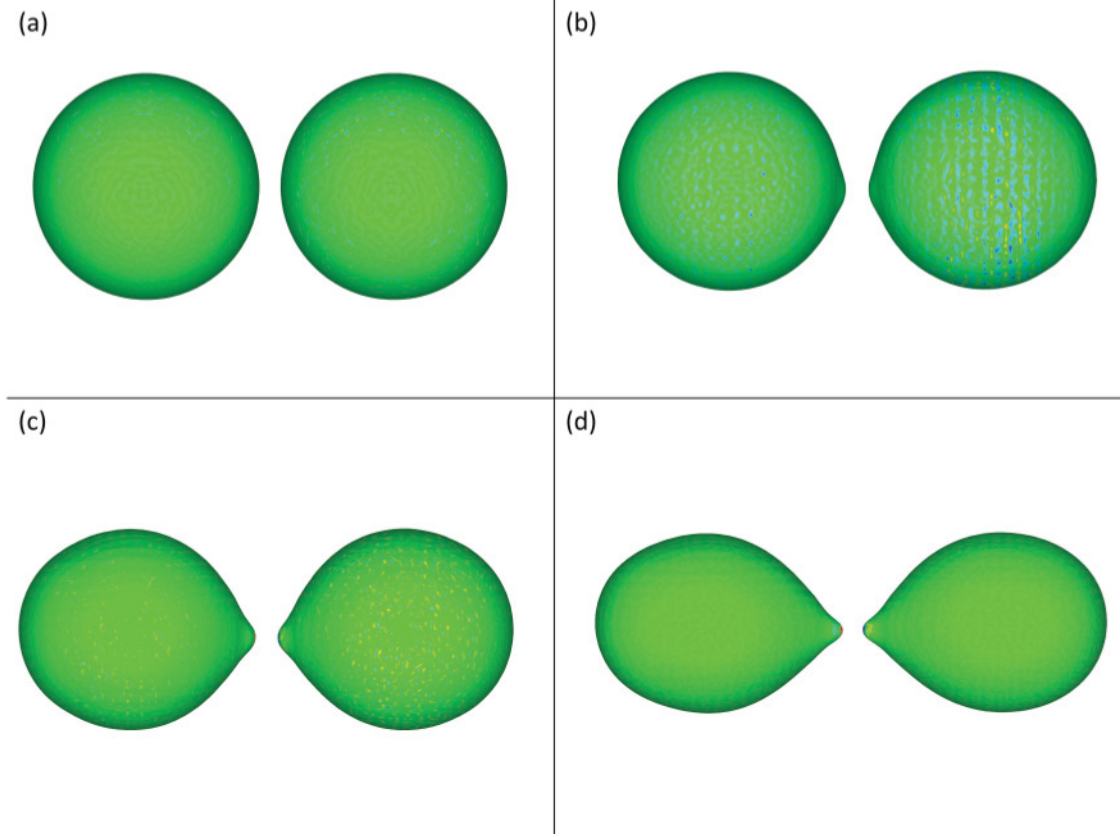


FIG. 7. (Color online) Initial cell shape (a) and cell shape at the time of bond rupture obtained from the IBM simulation of elastic cell with solid microvillus at $R_f = 10^5$ pN/s for (b) $E_h = 3.0$ dyn/cm, (c) $E_h = 1.2$ dyn/cm, and (d) $E_h = 0.3$ dyn/cm for the model parameters listed in Table I.

greater amount of time. In Fig. 5(c) we see that in the tethering regime the bond force increases linearly. More importantly, it is seen that if the microvillus viscosity is large enough, the force transferred to the bond approaches the magnitude of the applied load. If the microvillus viscosity is too low, there can be a significant difference between the instantaneous applied load and the force transmitted to the bond. Figure 5(d) shows that in the tethering regime the rate of microvillus extension increases as microvillus viscosity decreases.

D. Rupture force and time histograms

The impact of cell mechanics in modulating the transmission of the applied load to the molecular bond is seen in the histograms of rupture force shown in Fig. 6(a). Molecular bond rupture data is obtained through 10^5 Monte Carlo simulations based on the intermolecular bond force history obtained from the micromechanical model and IBM simulations at $R_f = 10^5$ pN/s for the model parameters listed in Table I. It is seen that the peak value of the rupture force histograms remains nearly unchanged when cellular and/or microvillus elasticity is introduced. The mean rupture force obtained from the simulation at $R_f = 10^5$ pN/s for various cell and microvillus models are tabulated in Table II. Once again, it is seen that the mean rupture force does not change significantly once elasticity is introduced. However, the peak and mean rupture time increase

as elasticity is introduced, as seen in Fig. 6(b) and Table II, respectively. The mean rupture force and time for the variation of microvillus parameters that were simulated to generate Figs. 4(a)–4(c) are reported in Table III. The observed variations in microvillus parameters do not lead to a significant change in the mean rupture force, as all calculated values are in the range 172.3–176.4 pN. However, the range of mean rupture time calculated was in the range of 2963.6–3289.4 μ s. In all cases we have used the Dembo slip model of the molecular bond with fixed kinetic parameters and applied an external load at a rate of $R_f = 10^5$ pN/s. Note that the probability density function for bond rupture given by

$$p(t, f) = k_r(f) \exp \left\{ - \int_0^t k_r[f(t')] dt' \right\}, \quad (22)$$

depends on the force history experienced by the molecular bond. We have demonstrated that cell and microvillus mechanics alter the transmission of force to the bond. Thus, different force histories lead to different statistics for bond rupture. It is interesting to note that for all mechanical models considered the range of mean rupture force observed was 157.7–176.4 pN, while the range of mean rupture times was 1593.2–3539.3 μ s. It is observed from Fig. 6 that the effect of increasing cellular elasticity on rupture force is weak while that on rupture time is stronger. The lowest values of mean rupture force and mean rupture time correspond to a solid cell with a solid microvillus. In this case, there is only a small lag time between the applied

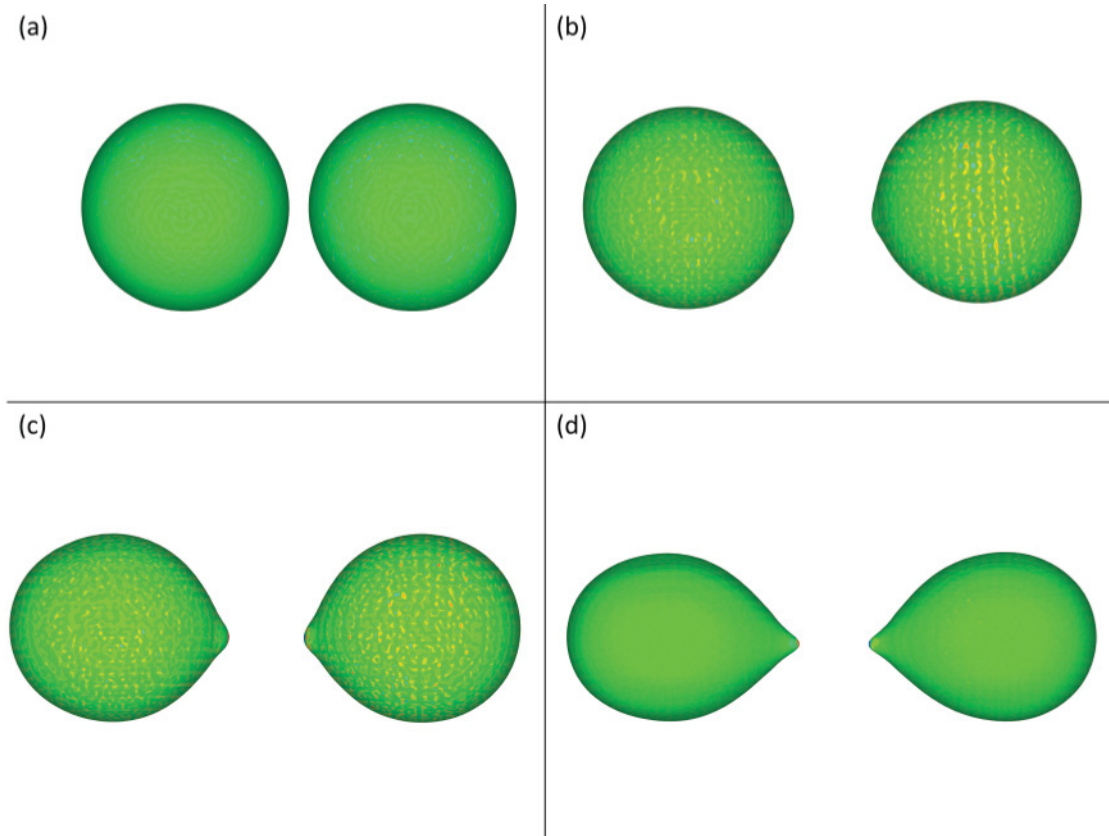


FIG. 8. (Color online) Initial cell shape (a) and cell shape at the time of bond rupture obtained from the IBM simulation of elastic cell with elastic microvillus at $R_f = 10^5$ pN/s for (b) $E_h = 3.0$ dyn/cm, (c) $E_h = 1.2$ dyn/cm, and (d) $E_h = 0.3$ dyn/cm for the model parameters listed in Table I.

force and the force transmitted to the molecular bond due to hydrodynamic drag on the cell. The calculated rupture mean rupture force and time for a solid cell–solid microvillus model are lower bounds for the quantities for a given loading rate. In our simulation we only saw the time lag increase as elasticity of the cell and the microvillus was introduced and we exclude the possibility of mechanisms that lead to force amplification. Given that biological cells are not solid, one expects the measured mean rupture force and mean rupture time to be larger than the lower bound for the solid model. The extent of the difference will depend on the deformability of the cell.

E. Effect of cell elasticity and microvillus viscoelasticity on cell shapes

While the purpose of DFS experiments is to measure the kinetic parameters of an intermolecular bond, it is challenging to measure the length of a bond and, more challenging, to measure the force exerted by a bond directly. By comparison, it is relatively easy to observe the effect of an intermolecular bond on a cell shape, which can be used to infer the extent of cell deformation. In Fig. 7(a) we show the initial spherical shape of cells prior to the application of external force $F(t)$ on the surface of each cell, while in Figs. 7(b)–7(d) we show the shape of the cells at the time of bond rupture. Deformed cell shapes shown in Figs. 7(b)–7(d) were obtained from 3D IBM

simulation of elastic cells for $E_h = 3.0, 1.2,$ and 0.3 dyn/cm with a solid microvillus at $R_f = 10^5$ pN/s, respectively. It is seen from these figures that cell deformation is concentrated in the bonding region due to highly localized stress prior to bond rupture. Further, it is noticed that cell deformation increases prior to bond rupture as we increase the membrane elasticity, i.e., as we decrease E_h . The corresponding cell shapes obtained from the simulation of elastic cells with a viscoelastic microvillus at $R_f = 10^5$ pN/s are shown in Figs. 8(a)–8(d). Once again it is seen that as we increase membrane elasticity, the cell deformation in the bond region increases prior to bond rupture. In fact, all the deformed cell shapes in Fig. 8 are nearly identical to the respective deformed cell shapes in Fig. 7, however, a careful comparison shows that the separation distance between the deformed cells is larger for a viscoelastic microvilli at the moment of bond rupture. This is attributed to the fact that force is transmitted to the molecular bond through microvillus extension, as discussed above.

IV. CONCLUSION

We have numerically investigated the effect of cell deformability and microvillus viscoelasticity on the transmission of an external cellular load to an intermolecular bond. These simulations successfully demonstrated that cell and microvillus deformation modulates the externally applied load such that the instantaneous intermolecular bond force

is not equivalent to the externally applied load. The time lag between the applied load and the intermolecular bond force is lowest when both the cell and microvillus are modeled as solid materials. Our simulations predict that both increased cell compliance and microvillus extensibility contribute to an increasing time lag between the instantaneous external cellular load and intermolecular bond force. The detachment of homotypic cells attached by a L-selectin and PSGL-1 bond as a function of the mechanical properties of both the cell and microvillus was simulated using a Monte Carlo method. The kinetic parameters of the bond model were held fixed across all cell and microvillus models. Bond lifetime and rupture force data sets were based on 10^5 simulations for each cell and microvillus model. For the fixed loading rate and models considered, it was found that the range of mean rupture force (based on bond length) observed was 157.7–176.4 pN, while the range of mean rupture times was 1593.2–3539.3 μ s,

implying that the effect of increasing cellular elasticity on rupture force is weak while that on rupture time is stronger. One would expect this because we are modeling the same bond. The lowest values of mean rupture force and mean rupture time correspond to a solid cell with a solid microvillus, while larger mean rupture forces and times correspond to more elastic cells. Through numerical simulation we have demonstrated that the statistical behavior of an intermolecular bond of fixed kinetic parameters is dependent on cell mechanics.

ACKNOWLEDGMENTS

The authors would like to acknowledge the financial support provided by the National Institute of Health Grant No. RO1 AI063366. We thank the Pittsburgh Supercomputing Center for computational resources under DAC allocation MCB090098.

-
- [1] E. A. Evans and D. A. Calderwood, *Science* **316**, 1148 (2007).
 [2] D. A. Simson, M. Strigl, M. Hohenadl, and R. Merkel, *Phys. Rev. Lett.* **83**, 652 (1999).
 [3] E. A. Evans and P. Williams, in *Physics of Bio Molecules and Cells*, edited by H. Flyvberg, F. Julicher, P. Ormos, and F. David (EDP Science/Springer, Paris, 2002), pp. 145–185.
 [4] D. F. Tees, R. E. Waugh, and D. A. Hammer, *Biophys. J.* **80**, 668 (2001).
 [5] S. Jadhav, C. D. Eggleton, and K. Konstantopoulos, *Biophys. J.* **88**, 96 (2005).
 [6] G. I. Bell, *Science* **200**, 618 (1978).
 [7] E. Evans, *Annu. Rev. Biophys. Biomol. Struct.* **30**, 105 (2001).
 [8] E. L. Florin, V. T. Moy, and H. E. Gaub, *Science* **264**, 415 (1994).
 [9] E. Evans and K. Ritchie, *Biophys. J.* **72**, 1541 (1997).
 [10] F. Kuhner, L. T. Costa, P. M. Bisch, S. Thalhammer, W. M. Heckl, and H. E. Gaub, *Biophys. J.* **87**, 2683 (2004).
 [11] J. Fritz, A. G. Katopodis, F. Kolbinger, and D. Anselmetti, *Proc. Natl. Acad. Sci. USA* **95**, 12283 (1998).
 [12] T. Yago, V. I. Zarnitsyna, A. G. Klopocki, R. P. McEver, and C. Zhu, *Biophys. J.* **92**, 330 (2007).
 [13] C. D. Paschall, W. H. Guilford, and M. B. Lawrence, *Biophys. J.* **94**, 1034 (2008).
 [14] E. A. Evans, A. Leung, D. Hammer, and S. Simon, *Proc. Natl. Acad. Sci. USA* **98**, 3784 (2001).
 [15] A. Rahman, Y. Tseng, and D. Wirtz, *Biochem. Biophys. Res. Commun.* **296**, 771 (2002).
 [16] R. Merkel, P. Nassoy, A. Leung, K. Ritchie, and E. Evans, *Nature (London)* **397**, 50 (1999).
 [17] S. E. Chesla, P. Selvaraj, and C. Zhu C, *Biophys. J.* **75**, 1553 (1998).
 [18] J. Y. Shao and J. B. Xu, *J. Biomech. Eng.* **124**, 388 (2002).
 [19] L. J. Rinko, M. B. Lawrence, and W. H. Guilford, *Biophys. J.* **86**, 544 (2004).
 [20] C. Gosse and V. Croquette, *Biophys. J.* **82**, 3314 (2002).
 [21] C. Haber and D. Wirtz, *Rev. Sci. Instrum.* **71**, 4561 (2000).
 [22] T. P. Tolentino, J. Wu, V. I. Zarnitsyna, Y. Fang, M. L. Dustin, and C. Zhu, *Biophys. J.* **95**, 920 (2008).
 [23] T. M. Dobrowsky, P. Panorchan, K. Konstantopoulos, and D. Wirtz, *Methods Cell Biol.* **89**, 411 (2008).
 [24] E. Reister-Gottfried, K. Sengupta, B. Lorz, E. Sackmann, U. Seifert, and A. S. Smith, *Phys. Rev. Lett.* **101**, 208103 (2008).
 [25] B. Różycki, R. Lipowsky, and T. R. Weikl, *Phys. Rev. Lett.* **96**, 048101 (2006).
 [26] B. T. Marshall, K. K. Sarangapani, J. Lou, R. P. McEver, and C. Zhu, *Biophys. J.* **88**, 1458 (2005).
 [27] Y. Zhang, G. Sun, S. Lu, N. Li, and M. Long, *Biophys. J.* **95**, 5439 (2008).
 [28] R. Alon, D. A. Hammer, and T. A. Springer, *Nature (London)* **374**, 539 (1995).
 [29] R. M. Raphael and R. E. Waugh, *Biophys. J.* **71**, 1374 (1996).
 [30] V. Heinrich, B. Božič, S. Svetina, and B. Žekš, *Biophys. J.* **76**, 2056 (1999).
 [31] Y. Chen, G. Girdhar, and J. Y. Shao, *Am. J. Physiol. Cell Physiol.* **292**, 1272 (2007).
 [32] J. Y. Shao, H. P. Ting Beall, and R. M. Hochmuth, *Proc. Natl. Acad. Sci. USA* **95**, 6797 (1998).
 [33] D. W. Schmidtke, and S. L. Diamond, *J. Cell Biol.* **149**, 719 (2000).
 [34] J. F. Mustard, M. A. Packham, R. L. Kinlough-Rathbone, D. W. Perry, and E. Regoeczi, *Blood* **52**(2), 453 (1978).
 [35] S. M. Albelda, *Lab. Invest.* **68**(1), 4 (1993).
 [36] E. Galkina and K. Ley, *Arterioscl. Throm. Vasc.* **27**, 2292 (2007).
 [37] L. Osborn, *Cell* **62**, 3 (1990).
 [38] M. B. Lawrence and T. A. Springer, *Cell* **65**, 859 (1991).
 [39] G. L. Nicolson, *Cancer Metastasis Rev.* **7**, 143 (1988).
 [40] L. A. Lasky, *Science* **258**, 964 (1992).
 [41] S. I. Simon and C. E. Green, *Annu. Rev. Biomed. Eng.* **7**, 151 (2005).
 [42] A. S. Smith, K. Sengupta, S. Goennenwein, U. Seifert, and E. Sackmann, *Proc. Natl. Acad. Sci. USA* **105**, 6906 (2008).
 [43] A. S. Smith, B. G. Lorz, S. Goennenwein, and E. Sackmann, *Biophys. J.* **90**, L52 (2006).
 [44] D. A. Hammer and S. M. Apte, *Biophys. J.* **63**, 35 (1992).
 [45] G. Girdhar, and Jin Yu Shao, *Biophys. J.* **93**, 4041 (2007).
 [46] T. A. Springer, *Cell* **76**, 301 (1994).

- [47] C. B. Korn and U. S. Schwarz, *Phys. Rev. E* **77**, 041904 (2008).
- [48] K. C. Chang and D. A. Hammer, *Biophys. J.* **79**, 1891 (2000).
- [49] K. C. Chang, D. F. Tees, and D. A. Hammer, *Proc. Natl. Acad. Sci. USA* **97**, 11262 (2000).
- [50] M. R. King and D. A. Hammer, *Biophys. J.* **81**, 799 (2001).
- [51] C. B. Korn and U. S. Schwarz, *Phys. Rev. Lett.* **97**, 138103 (2006).
- [52] C. B. Korn and U. S. Schwarz, *J. Chem. Phys.* **126**, 095103 (2007).
- [53] O. K. Dudko, G. Hummer, and A. Szabo, *Phys. Rev. Lett.* **96**, 108101 (2006).
- [54] G. Hummer and A. Szabo, *Biophys. J.* **85**, 5 (2003).
- [55] O. K. Dudko, A. E. Filippov, J. Klafter, and M. Urbakh, *Proc. Natl. Acad. Sci. USA* **100**, 11378 (2003).
- [56] R. B. Best, E. Paci, G. Hummer, and O. K. Dudko, *J. Phys. Chem. B* **112**, 5968 (2008).
- [57] E. Perret, A. Leung, H. Feracci, and E. Evans, *Proc. Natl. Acad. Sci. USA* **101**, 16472 (2004).
- [58] C. D. Eggleton and A. S. Popel, *Phys. Fluids* **10**, 1834 (1998).
- [59] M. Dembo, in *Lectures on Mathematics in the Life Sciences, Some Mathematical Problems in Biology*, Vol. 24 (American Mathematical Society, Providence, RI, 1994), pp. 51–77.
- [60] S. V. Marella and H. S. Udaykumar, *Phys. Fluids* **16**, 244 (2004).
- [61] C. S. Peskin and D. M. McQueen, *J. Comput. Phys.* **81**, 372 (1989).
- [62] S. Jadhav, K. Y. Chan, K. Konstantopoulos, and C. D. Eggleton, *J. Biomech.* **40**, 2891 (2007).
- [63] C. S. Peskin, *Acta Numer.* **11**, 479 (2002).
- [64] J. M. Charrier, S. Shrivastava, and R. Wu, *J. Strain Anal.* **24**, 55 (1989).
- [65] S. Shrivastava, and J. Tang, *J. Strain Anal.* **28**, 31 (1993).
- [66] E. Evans, A. Leung, V. Heinrich, and C. Zhu, *Proc. Natl. Acad. Sci. USA* **101**, 11281 (2004).
- [67] Y. V. Pereverzev, O. V. Prezhdo, M. Forero, E. V. Sokurenko, and W. E. Thomas, *Biophys. J.* **89**, 1446 (2005).
- [68] J. Li, M. Dao, C. T. Lim, and S. Suresh, *Biophys. J.* **88**, 3707 (2005).
- [69] M. L. Smith, M. J. Smith, M. B. Lawrence, and K. Ley, *Microcirculation* **9**(6), 523 (2002).
- [70] N. A. N'Dri, W. Shyy, and R. Tran Son Tay, *Biophys. J.* **85**, 2273 (2003).
- [71] J. L. Drury and M. Dembo, *Biophys. J.* **81**, 3166 (2001).
- [72] R. E. Bruehl, T. A. Springer, and D. F. Bainton, *J. Histochem. Cytochem.* **44**, 835 (1996).
- [73] Y. Zhao, S. Chien, and S. Weinbaum, *Biophys. J.* **80**, 1124 (2001).
- [74] J. Shillcock and U. Seifert, *Phys. Rev. E* **57**(6), 7301 (1998); O. K. Dudko, G. Hummer, and A. Szabo, *Phys. Rev. Lett.* **96**, 108101 (2006).
- [75] See Supplemental Material at <http://link.aps.org/supplemental/10.1103/PhysRevE.84.011912> for movies of elastic cells with solid and with elastic microvilli.
- [76] V. K. Gupta, I. A. Sraj, K. Konstantopoulos, and C. D. Eggleton, *Biomechan. Model. Mechanobiol.* **9**(5), 613 (2010).